High-Resolution Tunneling Spectroscopy of Fractional Quantum Hall States

Yuwen Hu[1†], Yen-Chen Tsui[1†], Minhao He[1†], Umut Kamber[1], Taige Wang[2], Amir S. Mohammadi[1], Kenji Watanabe[3], Takashi Taniguchi[4], Zlatko Papic[5], Michael P. Zaletel[2], Ali Yazdani[1*]

[1] Joseph Henry Laboratories and Department of Physics, Princeton University, Princeton, NJ 08544, USA

[2] Department of Physics, University of California at Berkeley, Berkeley, CA 94720, USA

[3] Research Center for Functional Materials, National Institute for Materials Science, 1-1 Namiki, Tsukuba 305-0044, Japan

[4] International Center for Materials Nanoarchitectonics, National Institute for Materials Science, 1-1 Namiki, Tsukuba 305-0044, Japan

[5] School of Physics and Astronomy, University of Leeds, Leeds LS2 9JT, UK

*Correspondence to: yazdani@princeton.edu

† These authors contributed equally to this work

Abstract:

Strong interaction among electrons in two-dimensional systems in the presence of high magnetic fields gives rise to fractional quantum Hall (FQH) states that host quasi-particles with fractional charge and statistics. We perform high-resolution scanning tunneling microscopy and spectroscopy of FQH states in ultra-clean Bernal-stacked bilayer graphene (BLG) devices. Spectroscopy of FQH states shows sharp excitations in tunneling experiments that have been predicted for electron fractionalizing into bound states of quasi-particles. From our measurements and their comparison to theoretical calculations, we find energy gaps for candidate non-abelian FQH states that are larger by a factor of 5 than other related systems, making BLG an ideal setting for the manipulation of these novel quasi-particles and for the creation of a topological quantum bit. Our STM experiment also reveals previously undiscovered states in such ultra-clean samples.

Main Text:

In two-dimensional (2D) systems, quenching electrons' kinetic energy with the application of large perpendicular magnetic fields enhances the interactions among electrons and drives the formation of fractional quantum Hall (FQH) states (*1*, *2*). FQH states and their low-energy excitations with anyonic statistics have been of interest for many decades (*3*–*6*); but there is renewed interest in such states because of their potential application for creating topologically protected qubits (*7–9*). Much of what is known about these states and their excitations has been obtained through macroscopically averaged experiments or studies of their edge states (*1*, *2*, *10–16*). Local spatially resolved experiments have the potential to probe exotic quasi-particles, determine sample quality, and achieve the ideal setting in which non-abelian anyons are long-lived for studies of their braiding statistics and for creating topological qubits. Local single electron transistor (SET) experiments have already been used to detect fractional charges (*17*, *18*), including $e/4$ charged quasi-particles in the even-denominator FQH states, which are the most promising candidate for hosting non-abelian anyons (*7*). New approaches for local detection of anyons and even testing their fusion rules have been proposed (*19*, *20*). Building on the recent success of atomic scale scanning tunneling microscopy and spectroscopy (STM/S) experiments to study quantum Hall states in monolayer graphene (*21*, *22*), here we show the application of these techniques to the myriad of FQH states in Bernal-stacked bilayer graphene (BLG). In this work, STM's ability to identify ultra-clean devices is harnessed to discover remarkably large energy gaps protecting FQH states, including those that are consistent with the proposed Moore-Read paired state hosting non-abelian anyons (*7*). Our tunneling spectroscopy experiments probe higher energy FQH's excitations, which are beyond the reach of transport studies, to reveal sharp peaks over narrow energies that have been predicted theoretically (*23*). Surprisingly, even though FQH states are highly correlated phases in which their low-energy excitations are distinct from electrons, high-energy composite states of fractionalized excitations have a strong overlap with electron or hole-like excitations. The ability to perform atomic scale imaging and spectroscopy allows us to probe the influence of single atomic defects and to characterize disorder-free intrinsic bulk properties of FQH states for the first time, which shows remarkably good agreement with theoretical calculations. The exponential suppression of thermally activated quasi-particles due to the large energy gaps reported here for the non-abelian states in BLG makes BLG an ideal platform for the realization of topological qubits based on non-abelian anyons.

The observation of FQH states is ubiquitous to materials platforms with 2D electronic states (*1*, *2*, *10–14*). However, their presence in graphene-based systems at the surface of devices, that can be made pristine on the atomic scale, makes high-resolution STM studies of FQH states possible (*21*, *24*). The Coulomb interaction in graphene-based systems in a magnetic field is also relatively stronger than, for example, that in GaAs because of the dielectric environment for these devices, making the energy scales for the formation of FQH states in graphene-based systems larger in comparison. Previous transport and electronic compressibility experiments have established that at partial filling of the lowest Landau levels (LLL) of BLG, in which the accidental degeneracy between orbital quantum number $N = 0$ and $N = 1$ LLs is lifted, this material system shows both odd (in $N = 0$) and even denominator FQH states (in $N = 1$) (*11*, *12*, *25–29*). Depending on experimental conditions, in particular the value of the displacement field perpendicular to the bilayer, this system can realize different broken symmetry states (*30*, *31*), from which various FQH states emerge (*12*, *25–29*). Although information about the broken symmetry states has been extracted from various macroscopically averaged experiments (*30*, *31*), visualization of such broken symmetry states, as recently achieved in monolayer graphene (*21*, *22*), has not been performed.

For our experiments, we fabricated BLG devices using hexagonal boron nitride (hBN) substrates with graphite back gates and performed various cleaning procedures to create devices with atomically pristine areas as large as $(200\ \text{nm})^2$, without any defects or adsorbates (see supplementary materials (SM) (*32*) for sample fabrication details). The STM topography of such ultra-clean devices shows the moiré pattern due to a mismatch of BLG and hBN lattices (~6.7 nm moiré periodicity) and very weak longer-range variations, see Fig. 1A and Fig. 1B for a device schematic and STM topography. Since the BLG in our devices is in an asymmetric dielectric environment (hBN on one side), we observe an energy splitting of U = 30 meV between the states occupying different layers (Fig. 1C). We attribute this to an effective intrinsic displacement field D_0, which induces a gap in the local density of states (LDOS) between the conduction and the valance band of BLG at zero magnetic field. As shown in Fig. 1C, the zero-field differential conductance d*I*/d*V* as a function of sample bias V_B measurements shows such a gap in the LDOS, which is independent of the gate voltage (V_G), except when we approach charge neutrality near $V_G = 0$, where it is strongly enhanced likely due to exchange effects (see Fig. S1 in (*32*) for larger gate range). A single particle calculation of the LDOS of the top layer BLG using a tight-binding model with an interlayer potential of $U = 30$ mV, due to D_0, can capture the gap and LDOS we observe at zero field away from charge neutrality (see SI discussion I, Fig. S2-3 in (*32*)). This comparison confirms that STM probes the electronic properties of BLG through measurements of the layer closest to the STM tip (layer separation is $d = 0.35$ nm). The corresponding $D_0 = \frac{\epsilon U}{d} = 343\ \text{mV/nm}$, if we assume a dielectric constant $\epsilon = 4$, is consistent with previous reports of similar device geometry (*12*, *33*), from which the D_0 (with $U = 30$ mV) is estimated to be about 300 mV/nm (*34*). Both numbers are much larger than the displacement field generated by back gate V_G in our studies. As we describe below, the presence of large intrinsic D_0 results in layer polarization of the FQH states and influences our STM measurements.

Application of a perpendicular magnetic field reconstructs the LDOS of BLG into discrete LLs, which appear as lines in density-dependent scanning tunneling spectroscopy (DD-STS) maps with 8 mV widths. With increasing V_G, after the LL closest to the Fermi energy (E_F) is filled, the higher LLs transit from unoccupied ($V_B > 0$) to occupied state ($V_B < 0$) (Fig. 1D at 5 T, see Fig. S4 in (*32*) for other fields). These transitions mark when each of the four-fold degenerate LLs, which we denote as filling factor ν = -8, -4, 4, 8 relative to charge neutrality, are fully occupied. Like previous work on monolayer graphene (*21*), tip preparation and sample cleanliness result in a minimal tip-gate effect (see SI Methods), as the LLs appear parallel to the V_G axis. These measurements show gapped integer quantum Hall (IQH) states as well as broken symmetry quantum Hall ferromagnetic (QHFM) phases when the four-fold degeneracy of the IQH states is lifted (*35*, *36*). From these features, the filling factor ν and the orbital number N can be determined (as labeled in Fig. 1D). Further analysis (right panel in Fig. 1D, also see discussion II, and Fig. S5 in (*32*)) shows the LLs energies to follow the expected $E_N =$

$\hbar\omega_c\sqrt{N(N-1)}$ sequence with extracted cyclotron gap $\hbar\omega_c$ at different fields (*37*, *38*), which also identifies different orbitals and yields an effective mass of $m^* \approx 0.044 m_e$, both consistent with previous studies (*37*, *39*). Details of the field dependence of various gaps are discussed in (*32*) (see Fig. S6).

We focus on the spectroscopic properties of the LLLs (N = 0, 1) by first examining signatures of layer polarization in the filling range $-4 < \nu < 4$, which has been explored in macroscopic measurements before (*31*) but can be visualized in our STM measurements. These experiments also determine the orbital states that are being filled which dictates the sequence of FQH states that can be formed at different fillings in BLG. As spectroscopic measurements show (at 10 T, Fig. 2A), for fillings $-4 < \nu < 0$ the LDOS near E_F of the top graphene layer, which is what STM probes in our experiments, is strongly suppressed relative to other energies. When a double peak feature (arrows in Fig. 2A near V_B = 30 to 40 mV) in these measurements, which appears above E_F for $\nu < 0$, crosses to the occupied states at $\nu = 0$, the LDOS at the E_F of the top layer is no longer suppressed. This behavior suggests that in the presence of intrinsic D_0, from the manifold of possible N = 0, 1 states, those that reside in the lower graphene layer of the BLG (Fig. 2B) are filled first for $\nu < 0$, thereby explaining why the LDOS near E_F measured on the top layer is suppressed in this regime. Once these levels are filled, the N = 0, 1 states of the top layer (double peak structure in Fig. 2A) cross the chemical potential and the LDOS near E_F begins to develop more spectral weight.

Another measurement that confirms this picture and provides further information on the sequence of orbital states being filled as a function of density is that of spectroscopic mapping of LLs in the top layer. As shown in Fig. 2B, the single-particle wave function of different orbital state N in each layer, $|\pm N\sigma\rangle$ ($\pm$ refers to K and K' valleys, and σ refers to spin) has different spectral weight on the four atomic sites of BLG (A, B, A' and B', as labeled in Fig. 2B). While the state $|-0\sigma\rangle$ has no spectral weight on the top layer, $|-1\sigma\rangle$ has some spectral weight on the B site of the top layer. We also note that the spectral weight from both LL orbitals in the top layer $|+N\sigma\rangle$ reside in the A sublattice of the top layer. We experimentally confirm this picture by finding that the relative weak spectral features near E_F for $\nu < 0$ (dashed orange box in Fig. 2A, which can be enhanced when the tip is closer to the sample) reside on B sublattice in spectroscopic maps (Fig. 2C left), while unoccupied levels just above E_F reside on A sublattice (Fig. 2C right). Not only do these measurements demonstrate that in the range $-4 < \nu < 0$ the system is polarized to fill the bottom graphene layer, but inspection of sublattice polarization in the range of $-3 < \nu < -2$ and $-1 < \nu < 0$ also shows sequential N = 0, 1, 0, 1 filling for the bottom layer for $\nu < 0$. Other measurements described below show that the same sequence of filling is followed for $0 < \nu < 4$, when the two orbitals in the top layer are filled. These findings are consistent with the high displacement field limit of a previous study (*31*).

Signatures of FQH states appear in high-resolution STM spectroscopy of LDOS near E_F, where experimental measurements are influenced by both the Coulomb gap (Δ_C) for the addition/removal of an electron to/from 2D systems at a high magnetic field (*21*, *40*–*42*) and the energy to create quasi-particles in various FQH states. The Coulomb gap arises because the low-energy excitations are orthogonal to the injection of a single electron (*43*). Figure 3A shows such measurements at 13.95 T for $0 < \nu < 1$, where we expect to fill the $|+0\sigma\rangle$ state, we find spectroscopic features at filling factors $\nu = \frac{p}{2p+1}$ ($p \in \mathbb{Z}$, with p up to 8 and -9) corresponding to the Jain sequence (two-flux composite fermions states) (*44*) that appear together with broad suppression near E_F corresponding to Δ_C. We find a similar sequence of FQH states features for -4 < ν < -3, -2 < ν < -1, and 2 < ν < 3 (See discussion III, Fig. S7-8 in (*32*)), where FQH states are observed at $\nu_{\text{eff}} \equiv \nu - \lfloor \nu \rfloor = \frac{p}{2p+1}$ at consecutive integer *p*, consistent with the expectation that $|\pm 0\sigma\rangle$ states are partially occupied at these fillings.

The onset of FQH states is accompanied by several distinct features in the high-resolution DD-STS measurements. First, we see that, in contrast with the tunneling spectra at partial fillings away from FQH states which show broad gap-like features associated with Δ_C, the FQH states are marked by enhanced threshold tunneling gaps Δ_t, which is flanked by sharp peaks in the spectra (see Fig. 3B, for example). Second, the additionally required charge excitation energy to add an electron (hole) can be evaluated by the sharp energy jumps Δ_e (Δ_h) upon entering (exiting) the incompressible FQH gaps. Third, these features occur over a gate range which, in the absence of impurity states, is directly related to the chemical potential jump $\delta\mu$ required to tune the system across these incompressible states' gaps (*45*). In the presence of impurities, the gate range can overestimate the chemical potential jump $\delta\mu$ and the associated thermodynamic gap. But as we describe below, our tunneling spectroscopy can be used to determine the role of in-gap states in our sample on the gate range required to tune across the thermodynamic gap, and place a lower bound on this gap in a realistic setting. We depict the key features of the spectra Δ_e, Δ_h, Δ_t, Δ_C, $\delta V_{G,h}$, $\delta V_{G,e}$ (there are slight differences between gate ranges for electron addition or removal), and the absolute value of the slope of spectroscopic features within the gate ranges $S_{G,h}$, $S_{G,e}$ in the schematic shown in the inset of Fig. 3D. While the jump in the chemical potential with the appearance of incompressible FQH state is not surprising, the observation that FQH states, which do not have electron-like low energy quasi-particles, show sharp resonances in electron tunneling spectra is remarkable. Previous theoretical studies had anticipated that such sharp features in tunneling experiments may occur as high angular momentum excitations of fractional quasi-particles of FQH states (*23*); however, they have not been detected in any previous tunneling spectroscopy experiments. Conceptually, the added tunneling electron (hole) can be thought to be transformed into composite states of $2p + 1$ fractional quasi-particles (quasi-holes) and the Coulomb repulsion among which is compensated by them being in a high angular momentum state (*23*, *40*, *43*).

A natural question that arises is whether the activated conductivity of the FQH state can result in voltage division of V_B between the tip-sample junction resistance and intrinsic resistance of the sample, thereby influencing FQH features in the STM spectroscopic measurements. To address this concern, we have carried out experiments at different tip-sample separations, in which we are changing the relative ratio of tip-sample resistance to that of the sample (See Fig. S9-10). We find all the features of FQH states, and particularly the onset of tunneling current within the incompressible region of gate voltages, to remain independent of the junction resistance (Fig. S9). Unlike transport studies, we are not probing FQH states with low-energy quasi-particles, but with multiple high-energy quasi-particles created by the decay of a tunneling electron (with its energy greater than the Coulomb gap). These quasi-particles are created at energies of several meVs and can transport the small tunneling current to the contacts. The quasi-particle transport also occurs in transport experiments when they are thermally excited and results in finite transport currents at low bias. Since the tunneling currents are small, we are exciting the system with a small density of energetic quasi-particles that decay away from the tip before the next tunneling event.

For more quantitative analysis of our spectroscopic measurements FQH states, we extract from our DD-STS measurements the values of Δ_e, Δ_h, Δ_t, Δ_C, $\delta V_{G,h}$, $\delta V_{G,e}$, $S_{G,h}$ and $S_{G,e}$, (at B =13.95 T) for all the odd denominator FQH states in the range $0 < \nu < 1$ (See Method in (*32*) for the details of extractions). Examining measurements at different fields (see Fig. S11 in (*32*)), we find that Δ_C follows the expected $\sqrt{B}$ behavior of the Coulomb energy (*40*), while the Δ_t of the various FQH states systematically increases in its magnitude beyond Δ_C in a linear fashion with B field (see Fig. 3C). Motivated by clear enhancement beyond Δ_C for tunneling into the FQH states, we plot $\Delta_e + \Delta_h$ as a function of p (where $p = \frac{\nu}{1-2\nu}$) and find its systematic suppression with increasing $|p|$ (Fig. 3D). An interesting experimental finding is that $\Delta_e + \Delta_h$ follows a trend of $\frac{1}{|2p+1|}$ as a function of p (Fig. 3D green solid lines) except for ν = 2/3 state where the gap is anomalously large. This p dependence resembles the previously predicted trend for the gap to create a quasi-particle-quasi-hole pair for the odd denominator FQH states within the composite fermions (CF) theory (*46*, *47*). This quantitative agreement requires further investigation. The observations of a combination of sharp features in spectroscopy and the hierarchy of $\Delta_e + \Delta_h$ among the odd denominator FQH states demonstrate a new spectroscopic approach for studying these states by characterizing the process of fractionalizing the tunneling electron (hole) into quasi-particles (hole) of FQH states.

The local measurements of $\delta V_{G,avg} = (\delta V_{\mathrm{G,e}} + \delta V_{\mathrm{G,h}})/2$, which shows a similar trend as a function of $|p|$ (See Fig. S12), can be analyzed to characterize $\delta\mu/e$ and the thermodynamic gaps for various FQH states even in the realistic setting where there is a background of impurities in the sample. In the absence of any impurities, $e\delta V_{\mathrm{G,avg}} \sim \delta\mu$, and changing the gate voltage would shift the chemical potential of the sample in such a way that all features in the incompressible state shift linearly with slope $S_{\mathrm{G},e} = S_{\mathrm{G},h} = 1$ as a function of the gate voltage. However, in the presence of any impurities that can electrostatically influence the areas under the tip (which can be one in a few hundred nm square areas, see SI section V and below), sweeping the gate voltage fills these states and in turn changes the slope S_{G} to be less than one. Using the combination of measurements to determine the product $eS_G\delta V_G = e(S_{G,e}\delta V_{G,e} + S_{G,h}\delta V_{G,h})/2$ puts a lower bound on the thermodynamic gaps $\delta\mu$ for various FQH states in the realistic setting of the sample with a finite concentration of defects (Fig. 3D and SI section V). The almost perfect correspondence between $(\Delta_e + \Delta_h)/2$ and $eS_G\delta V_G$ as is apparent from Fig. 3D makes sense since the Coulomb gap is more or less the same as we sweep the gate voltage through the incompressible states and suggest that the jumps $\varDelta_e, \varDelta_h$ are also related to the jump in the chemical potential associated with the thermodynamic gap (modified in a realistic setting by the in-gap states).

Extending our measurements to when $|\pm 1\sigma\rangle$ states are being filled, we find spectroscopic signatures of the exotic even-denominator FQH states, a different hierarchy of quasi-particle excitation gaps, as well as some unexpected FQH states. As shown in Fig. 4A, in the range $-1 < \nu < 0$ when filling $|-1\sigma\rangle$ state, a pronounced even denominator state (ν_{eff} = 1/2) in the spectroscopy measurements is flanked by other FQH states (inset of Fig. 4A). The extracted $eS_{\mathrm{G}}\delta V_{\mathrm{G}}$ corresponding to the lower bound of the thermodynamic gaps for this sequence of FQH states shown in Fig. 4B show several remarkable features. First, the appearance of ν_{eff} = 1/2 flanked by ν_{eff} = 8/17 and 7/13 strongly suggests that the even denominator state corresponds to the non-abelian Moore-Read Pfaffian state (*7*), together with its Levin-Halperin daughter states forming on its sides (*48*). This observation (and lack of any features at ν_{eff} = 9/17 and 6/13) is also consistent with transport and compressibility studies (*28*, *29*) favoring Pfaffian, over anti-Pfaffian (*49*) or PH-Pfaffian (*50*), in the BLG. However, the second important feature of the data in Fig. 4B is that both the $(\varDelta_e + \varDelta_h)/2$, as well as the lower bound on the thermodynamic gap $eS_G\delta V_{\mathrm{G}}$ for the measured ν_{eff} = 1/2 locally (Fig. 4C) are a factor of 5 larger than those from previously reported macroscopically averaged experiments (*26*, *28*). Other remarkable features of the data in Fig. 4A are the observation of ν_{eff} = 2/5 and 3/5 states that may be Jain sequence due to a small mixture of *N* = 0 state or the predicted Read-Rezayi states (*51*), which like the Moore-Read state are also expected to be non-abelian (*52*). There is also the observation of new and unexpected FQH states at ν_{eff} = 5/11, 6/11, and 5/9. The gap size hierarchy of these FQH states (determined from $eS_{\mathrm{G}}\,\delta V_{\mathrm{G}}$) which decreases when moving away from ν_{eff} = 1/2 suggests that they could be also related to the even-denominator state. Experiments at fillings $-3 < \nu < -2$, $1 < \nu < 2$, and $3 < \nu < 4$ all show clear signatures of even-denominator states, with the latter two ranges also showing clear signatures of daughter states consistent with the even-denominator states being Pfaffian (see section IV, and Fig. S13-15 in (*32*)).

A natural question is how the properties of FQH states vary spatially and what are the typical spatial variation of our spectroscopic measurements in our BLG samples. In general, we find that the moiré structure due to h-BN underneath does not affect our measurement. However, in some regions of the sample, there are long-range variations of the spectra, which in some cases can be clearly attributed to the dilute concentration of defects in our sample. For example, Fig. 4D, 4E show that a sub-surface defect locally suppresses the even-denominator state with the $\varDelta_t$ recovering from on the scale of 100 nm away (Fig. S16 in (*32*)). Future studies can use spatial resolved spectroscopy to further investigate the distribution of such variations and the impact of the proximity of various impurities in the sample to each other on the spectroscopic properties of FQH states. The concentration of defects observed in our field of view also provides a consistent picture of how these states influence the gate range for being in the incompressible gap as described above (See SI section V).

The remarkably large energy scales for quasi-particle excitations and lower bounds on thermodynamic gaps we have extracted from our measurements away from any defects in our ultra-clean samples suggest that we are probing FQH states with unprecedented precision, thereby motivating comparison of our results with those of idealized theoretical calculations. Numerical simulation of the LDOS using screened Coulomb interactions that are appropriate for our one-sided-hBN and a single gate can be performed within the standard framework for describing FQH states (see section VI in (*32*)). The exact diagonalization (ED) calculations show signatures of the sharp features similar to our tunneling experiments (Fig. S17 in (*32*)), and the tunneling threshold energy on different system sizes that can be used to determine Δ_t in the limit of large system size (Fig. S20 in (*32*)). Given that the theory ignores the particle-hole asymmetry, we compare the theoretical results with the average value of the experimentally measured Δ_t for two equivalent FQH states relative to half-filling. In Fig. 4F, we show that using a reasonable value for the dielectric constant ϵ, we find measurements of Δ_t for FQH states in both $N = 0$ and 1 states are in excellent agreement with theory (see section VIII, Fig. S8C, S13D, S14D, S15D, Table S10 in (*32*) for comparison at other fillings and see section VIII, Table S9 in (*32*) for small changes in ϵ as a function of LL fillings). Similarly, we can compare our measurements of $eS_{\mathrm{G}}\,\delta V_{\mathrm{G}}$ for some of the FQH states to ED and the density matrix renormalization group (DMRG) calculation of the thermodynamic gaps and find them to somewhat smaller than the idealized situation as expected (see section VI, VII, and VIII, Table S11 in (*32*)). However, the remarkably large lower bound of thermodynamic gaps for exotic FQH states, such as close to 19 K for the Moore-Read states in our local measurements of ultra-clean BLG devices show that this is an ideal system for exploring the properties of the predicted non-abelian anyons. In ultra-clean GaAs devices (*53*), the gaps for such states realized at $\nu = 5/2$ are about a factor of 5 smaller. Future STM experiments in ultra-clean BLG samples can utilize electrostatic confining potentials to directly visualize the fractionalization process which has unique signatures for each FQH state (*20*).

STM studies also provide a more precise way to characterize FQH states, as well as an opportunity to find previously undiscovered states. In GaAs, estimates of the bulk gap for the FQH state from transport studies have been consistently smaller than those predicted theoretically (*54*), likely because such measurements are sensitive to disorder in the sample (*55*) (see above for an example of the local influence of individual impurities on FQH gaps, and Fig. S16 in (*32*), as well as discussion on the influence of in-gap states on estimating the lower bound on thermodynamic gaps). A coincident experiment (*56*) reports the thermodynamic gaps for the FQH states examined here in ultra-clean devices of BLG, where they find comparable gaps using a graphene sensor, to our lower bound of thermodynamic gap for the Jain sequence reported in here (see SI Fig. S27). Our measurements of 1/2 state locally with the STM still find a larger lower bound compared to these measurements, a behavior that is not surprising given that STM can make measurements in locations that are furthest away from defects to find the best experimental conditions closest to the idealized conditions for this state, which could be more sensitive to local disorder.

STM's ability to probe the disorder-free areas of the sample can also uncover new FQH states. We encountered an example of such a finding while probing the higher $N = 2$ LL, where we find not only a rich sequence of odd denominator states (*33*) but also an unexpected even denominator FQH state (Fig. 5A). While the even denominator FQH state in higher LLs has been reported in monolayer graphene (*57*), it is the first time such a state has been observed in a higher-LL of BLG. The hierarchy of local gaps (Fig. 5B) suggests the odd denominator FQH states are the composite fermion states. Interestingly, both $\Delta_e + \Delta_h$ and $eS_G\delta V_G$ are more particle-hole symmetric with respect to half filling than in the LLLs, consistent with the previous report (*33*). Different from the stripe phase observed in higher LLs in GaAs (*58*, *59*), the new even denominator FQH state may be due to either Moore-Read (*7*, *52*), parton 221 state (*57*) or other exotic composite fermion paired state (*60*). The exact isospin flavor, the role of the $N = 2$ LL's spinor structure and a microscopic description of such a state remain interesting open questions. Overall, our studies established that ultra clean BLG is an ideal platform for future local experiments on FQH states and for potentially creating a topological qubit using local manipulation of non-abelian anyons in the even-denominator FQH states.

Note: After submission of this manuscript, we became aware of a recent report (*61*) on realizing an even-denominator state in GaAs wide quantum wells, which effectively forms a quantum Hall bilayer with inter-layer tunneling, suggesting a more robust route to non-abelian anyons in GaAs. Despite the seeming similarity to BLG, we note the microscopic origin of these states is different: in wide quantum wells the fractional filling lies in two nearly degenerate $N = 0$ LLs, while in BLG this and previous works (*26*, *28*, *31*) establishes the 1/2 state occupies a single, isospin-polarized $N = 1$ LL.

References

1. D. C. Tsui, H. L. Stormer, A. C. Gossard, Two-dimensional magnetotransport in the extreme quantum limit. *Phys Rev Lett*. **48**, 1559 (1982).
2. R. Willett, J. P. Eisenstein, H. L. Störmer, D. C. Tsui, A. C. Gossard, J. H. English, Observation of an even-denominator quantum number in the fractional quantum Hall effect. *Phys Rev Lett*. **59**, 1776 (1987).
3. R. De-Picciotto, M. Reznikov, M. Heiblum, V. Umansky, G. Bunin, D. Mahalu, Direct observation of a fractional charge. *Nature* **389**, 162–164 (1997).
4. J. Nakamura, S. Liang, G. C. Gardner, M. J. Manfra, Direct observation of anyonic braiding statistics. *Nat Phys*. **16**, 931–936 (2020).
5. H. Bartolomei, M. Kumar, R. Bisognin, A. Marguerite, J.-M. Berroir, E. Bocquillon, B. Placais, A. Cavanna, Q. Dong, U. Gennser, others, Fractional statistics in anyon collisions. *Science* **368**, 173–177 (2020).

6. B. Dutta, W. Yang, R. Melcer, H. K. Kundu, M. Heiblum, V. Umansky, Y. Oreg, A. Stern, D. Mross, Distinguishing between non-abelian topological orders in a quantum Hall system. *Science* **375**, 193–197 (2022).
7. G. Moore, N. Read, Nonabelions in the fractional quantum Hall effect. *Nucl Phys B*. **360**, 362–396 (1991).
8. A. Y. Kitaev, Fault-tolerant quantum computation by anyons. *Ann Phys (N Y)*. **303**, 2–30 (2003).
9. C. Nayak, S. H. Simon, A. Stern, M. Freedman, S. Das Sarma, Non-Abelian anyons and topological quantum computation. *Rev Mod Phys*. **80**, 1083–1159 (2008).
10. K. I. Bolotin, F. Ghahari, M. D. Shulman, H. L. Stormer, P. Kim, Observation of the fractional quantum Hall effect in graphene. *Nature*. **462**, 196–199 (2009).
11. D. K. Ki, V. I. Fal'Ko, D. A. Abanin, A. F. Morpurgo, Observation of even denominator fractional quantum hall effect in suspended bilayer graphene. *Nano Lett*. **14**, 2135–2139 (2014).
12. A. Kou, B. E. Feldman, A. J. Levin, B. I. Halperin, K. Watanabe, T. Taniguchi, A. Yacoby, Electron-hole asymmetric integer and fractional quantum Hall effect in bilayer graphene. *Science* **345**, 55–57 (2014).
13. J. Falson, D. Maryenko, B. Friess, D. Zhang, Y. Kozuka, A. Tsukazaki, J. H. Smet, M. Kawasaki, Even-denominator fractional quantum Hall physics in ZnO. *Nat Phys*. **11**, 347–351 (2015).
14. Q. Shi, E. M. Shih, M. V. Gustafsson, D. A. Rhodes, B. Kim, K. Watanabe, T. Taniguchi, Z. Papić, J. Hone, C. R. Dean, Odd- and even-denominator fractional quantum Hall states in monolayer WSe2. *Nat Nanotechnol*. **15**, 569–573 (2020).
15. M. Banerjee, M. Heiblum, V. Umansky, D. E. Feldman, Y. Oreg, A. Stern, Observation of half-integer thermal Hall conductance. *Nature*. **559**, 205–210 (2018).
16. H. K. Kundu, S. Biswas, N. Ofek, V. Umansky, M. Heiblum, Anyonic interference and braiding phase in a Mach-Zehnder Interferometer. *Nat Phys*. **19**, 515–521 (2023).
17. J. Martin, S. Ilani, B. Verdene, J. Smet, V. Umansky, D. Mahalu, D. Schuh, G. Abstreiter, A. Yacoby, Localization of fractionally charged quasi-particles. *Science* **305**, 980–983 (2004).
18. V. Venkatachalam, A. Yacoby, L. Pfeiffer, K. West, Local charge of the $\nu = 5/2$ fractional quantum Hall state. *Nature*. **469**, 185–188 (2011).
19. B. Van Heck, M. Burrello, A. Yacoby, A. R. Akhmerov, Topological blockade and measurement of topological charge. *Phys Rev Lett*. **110**, 86803 (2013).
20. Z. Papić, R. S. K. Mong, A. Yazdani, M. P. Zaletel, Imaging anyons with scanning tunneling microscopy. *Phys Rev X*. **8**, 11037 (2018).
21. X. Liu, G. Farahi, C.-L. Chiu, Z. Papic, K. Watanabe, T. Taniguchi, M. P. Zaletel, A. Yazdani, Visualizing broken symmetry and topological defects in a quantum Hall ferromagnet. *Science* **375**, 321–326 (2022).
22. A. Coissard, D. Wander, H. Vignaud, A. G. Grushin, C. Repellin, K. Watanabe, T. Taniguchi, F. Gay, C. B. Winkelmann, H. Courtois, Hermann Sellier, Benjamin Sacépé,

Imaging tunable quantum Hall broken-symmetry orders in graphene. *Nature*. **605**, 51–56 (2022).
23. J. K. Jain, M. R. Peterson, Reconstructing the electron in a fractionalized quantum fluid. *Phys Rev Lett*. **94**, 186808 (2005).
24. G. M. Rutter, S. Jung, N. N. Klimov, D. B. Newell, N. B. Zhitenev, J. A. Stroscio, Microscopic polarization in bilayer graphene. *Nat Phys*. **7**, 649–655 (2011).
25. P. Maher, L. Wang, Y. Gao, C. Forsythe, T. Taniguchi, K. Watanabe, D. Abanin, Z. Papić, P. Cadden-Zimansky, J. Hone, others, Tunable fractional quantum Hall phases in bilayer graphene. *Science* **345**, 61–64 (2014).
26. J. I. A. Li, C. Tan, S. Chen, Y. Zeng, T. Taniguchi, K. Watanabe, J. Hone, C. R. Dean, Even-denominator fractional quantum Hall states in bilayer graphene. *Science* **358**, 648–652 (2017).
27. Y. Kim, D. S. Lee, S. Jung, V. Skákalová, T. Taniguchi, K. Watanabe, J. S. Kim, J. H. Smet, Fractional quantum Hall states in bilayer graphene probed by transconductance fluctuations. *Nano Lett*. **15**, 7445–7451 (2015).
28. A. A. Zibrov, C. Kometter, H. Zhou, E. M. Spanton, T. Taniguchi, K. Watanabe, M. P. Zaletel, A. F. Young, Tunable interacting composite fermion phases in a half-filled bilayer-graphene Landau level. *Nature*. **549**, 360–364 (2017).
29. K. Huang, H. Fu, D. R. Hickey, N. Alem, X. Lin, K. Watanabe, T. Taniguchi, J. Zhu, Valley isospin controlled fractional quantum hall states in bilayer graphene. *Phys Rev X*. **12**, 31019 (2022).
30. Y. Zhao, P. Cadden-Zimansky, Z. Jiang, P. Kim, Symmetry breaking in the zero-energy Landau level in bilayer graphene. *Phys Rev Lett*. **104**, 66801 (2010).
31. B. M. Hunt, J. I. A. Li, A. A. Zibrov, L. Wang, T. Taniguchi, K. Watanabe, J. Hone, C. R. Dean, M. Zaletel, R. C. Ashoori, others, Direct measurement of discrete valley and orbital quantum numbers in bilayer graphene. *Nat Commun*. **8**, 948 (2017).
32. See supplementary materials.
33. G. Diankov, C.-T. Liang, F. Amet, P. Gallagher, M. Lee, A. J. Bestwick, K. Tharratt, W. Coniglio, J. Jaroszynski, K. Watanabe, others, Robust fractional quantum Hall effect in the N= 2 Landau level in bilayer graphene. *Nat Commun*. **7**, 13908 (2016).
34. Y. Zhang, T. T. Tang, C. Girit, Z. Hao, M. C. Martin, A. Zettl, M. F. Crommie, Y. R. Shen, F. Wang, Direct observation of a widely tunable bandgap in bilayer graphene. *Nature*. **459**, 820–823 (2009).
35. Y. Barlas, R. Côté, K. Nomura, A. H. MacDonald, Intra-Landau-level cyclotron resonance in bilayer graphene. *Phys Rev Lett*. **101**, 97601 (2008).
36. J. Lambert, R. Côté, Quantum Hall ferromagnetic phases in the Landau level N= 0 of a graphene bilayer. *Phys Rev B*. **87**, 115415 (2013).
37. E. McCann, V. I. Fal'ko, Landau-level degeneracy and quantum Hall effect in a graphite bilayer. *Phys Rev Lett*. **96**, 86805 (2006).

38. L.-J. Yin, S.-Y. Li, J.-B. Qiao, J.-C. Nie, L. He, Landau quantization in graphene monolayer, Bernal bilayer, and Bernal trilayer on graphite surface. *Phys Rev B*. **91**, 115405 (2015).
39. K. Zou, X. Hong, J. Zhu, Effective mass of electrons and holes in bilayer graphene: Electron-hole asymmetry and electron-electron interaction. *Phys Rev B*. **84**, 85408 (2011).
40. J. P. Eisenstein, L. N. Pfeiffer, K. W. West, Coulomb barrier to tunneling between parallel two-dimensional electron systems. *Phys Rev Lett*. **69**, 3804 (1992).
41. O. E. Dial, R. C. Ashoori, L. N. Pfeiffer, K. W. West, High-resolution spectroscopy of two-dimensional electron systems. *Nature*. **448**, 176–179 (2007).
42. O. E. Dial, R. C. Ashoori, L. N. Pfeiffer, K. W. West, Anomalous structure in the single particle spectrum of the fractional quantum Hall effect. *Nature*. **464**, 566–570 (2010).
43. S. He, P. M. Platzman, B. I. Halperin, Tunneling into a two-dimensional electron system in a strong magnetic field. *Phys Rev Lett*. **71**, 777 (1993).
44. J. K. Jain, Composite-fermion approach for the fractional quantum Hall effect. *Phys Rev Lett*. **63**, 199 (1989).
45. G. Farahi, C.-L. Chiu, X. Liu, Z. Papic, K. Watanabe, T. Taniguchi, M. P. Zaletel, A. Yazdani, Broken symmetries and excitation spectra of interacting electrons in partially filled Landau levels. *Nat. Phys.* 19, 1482-1488 (2023).
46. B. I. Halperin, Theory of the quantized Hall conductance. *Helvetica Physica Acta*. **56**, 75–102 (1983).
47. R. H. Morf, N. d'Ambrumenil, S. Das Sarma, Excitation gaps in fractional quantum Hall states: An exact diagonalization study. *Phys Rev B*. **66**, 75408 (2002).
48. M. Levin, B. I. Halperin, Collective states of non-Abelian quasiparticles in a magnetic field. *Phys Rev B*. **79**, 205301 (2009).
49. E. H. Rezayi, Landau level mixing and the ground state of the ν= 5/2 quantum Hall effect. *Phys Rev Lett*. **119**, 26801 (2017).
50. P. T. Zucker, D. E. Feldman, Stabilization of the particle-hole Pfaffian order by Landau-level mixing and impurities that break particle-hole symmetry. *Phys Rev Lett*. **117**, 96802 (2016).
51. N. Read, E. Rezayi, Beyond paired quantum Hall states: Parafermions and incompressible states in the first excited Landau level. *Phys Rev B*. **59**, 8084 (1999).
52. Z. Papić, D. A. Abanin, Y. Barlas, R. N. Bhatt, Tunable interactions and phase transitions in Dirac materials in a magnetic field. *Phys Rev B*. **84**, 241306 (2011).
53. Y. J. Chung, K. A. Villegas Rosales, K. W. Baldwin, P. T. Madathil, K. W. West, M. Shayegan, L. N. Pfeiffer, Ultra-high-quality two-dimensional electron systems. *Nat Mater*. **20**, 632–637 (2021).
54. T. Zhao, K. Kudo, W. N. Faugno, A. C. Balram, J. K. Jain, Revisiting excitation gaps in the fractional quantum Hall effect. *Phys Rev B*. **105**, 205147 (2022).
55. N. d'Ambrumenil, B. I. Halperin, R. H. Morf, Model for dissipative conductance in fractional quantum Hall states. *Phys Rev Lett*. **106**, 126804 (2011).

56. A. Assouline, H. Zhou, T. Wang, L. A. Cohen, F. Yang, R. Bai, T. Taniguchi, K. Watanabe, M. P. Zaletel, A. F. Young, Thermodynamic and activation gaps of fractional quantum Hall states in bilayer graphene. *Physical Review Letters* 132, 046603 (2024).
57. Y. Kim, A. C. Balram, T. Taniguchi, K. Watanabe, J. K. Jain, J. H. Smet, Even denominator fractional quantum Hall states in higher Landau levels of graphene. *Nat Phys*. **15**, 154–158 (2019).
58. M. P. Lilly, K. B. Cooper, J. P. Eisenstein, L. N. Pfeiffer, K. W. West, Evidence for an anisotropic state of two-dimensional electrons in high Landau levels. *Phys Rev Lett*. **82**, 394 (1999).
59. R. R. Du, D. C. Tsui, H. L. Stormer, L. N. Pfeiffer, K. W. Baldwin, K. W. West, Strongly anisotropic transport in higher two-dimensional Landau levels. *Solid State Commun*. **109**, 389–394 (1999).
60. A. Sharma, S. Pu, A. C. Balram, J. K. Jain, Fractional quantum Hall effect with unconventional pairing in monolayer graphene. *Phys Rev Lett*. **130**, 126201 (2023).
61. S. K. Singh, C. Wang, C. T. Tai, C. S. Calhoun, A. Gupta, K. W. Baldwin, L. N. Pfeiffer, M. Shayegan, Topological phase transition between composite-fermion and Pfaffian daughter states near $\nu = 1/2$ FQHS. *arXiv*: 2309. 00111 (2023).

Acknowledgments:

We thank useful conversations with Andrea Young and Amir Yacoby.

Funding:

This work was primarily supported by DOE-BES grant DE-FG02-07ER46419 the Gordon and Betty Moore Foundation’s EPiQS initiative grants GBMF9469 to A.Y. Other support for the experimental work was provided by NSF-MRSEC through the Princeton Center for Complex Materials NSF-DMR- 2011750, NSF-DMR-1904442, ARO MURI (W911NF-21-2-0147), and ONR N00012-21-1-2592. A.Y. acknowledge the hospitality of the Aspen Center for Physics, which is supported by National Science Foundation grant PHY-1607611, where part of this work was carried out. M.Z. and T.W. are supported by the U.S. Department of Energy, Office of Science, Office of Basic Energy Sciences, Materials Sciences and Engineering Division, under Contract No. DE-AC02-05CH11231, within the van der Waals Heterostructures Program (KCWF16). Z.P. acknowledges support by the Leverhulme Trust Research Leadership Award RL-2019-015 and in part by the National Science Foundation under Grant No. NSF PHY-1748958.

Author contributions:

YH, Y-CT, MH, UK, AY devised the experiments, with YH, Y-CT, MH, and UK created devices structures and carried out the STM measurements and data analysis. AM, TW, ZP, and

MZ carried out the theoretical calculations. KW, and TT provided the h-BN substrates. YH, Y-CT, MH, AY, TW, ZP, MZ all collaborated in writing of the manuscript.

Competing interests:

Authors declare no competing interests.

Data and materials availability:

All data, code, and materials used in the analysis will be made available for purposes of reproducing or extending the analysis. All data are available in the main text or the supplementary materials.

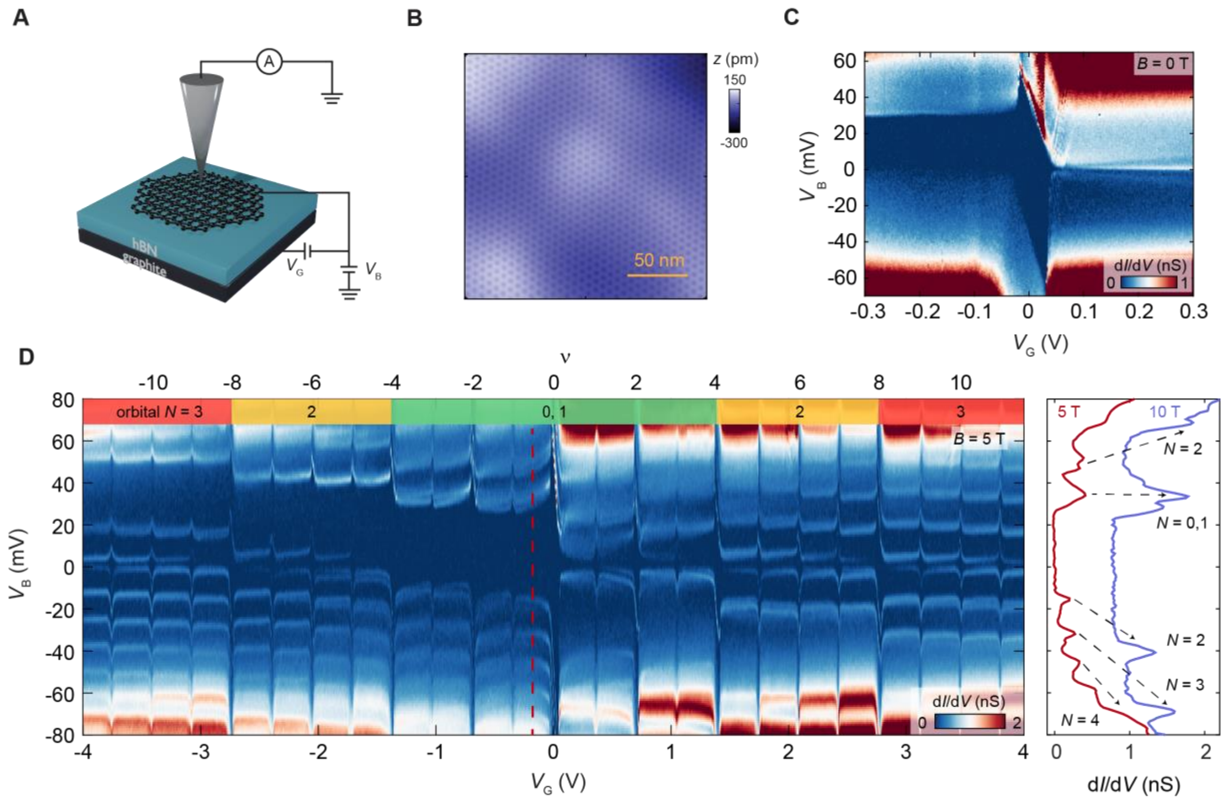

Fig. 1. Experimental setup and tunneling spectra at zero and low magnetic fields. **(A)** The schematic of the bilayer graphene device and the STM/STS experimental setup. A bias voltage V_B is applied to BLG to enable tip-sample tunneling. A voltage $V_G + V_B$ is applied to the bottom graphite gate to electrostatically tune the carrier density**. (B)** The topography image of the ultra-clean bilayer graphene device. The scale bar is 50 nm. **(C)** The tunneling spectra at zero magnetic field B = 0 T. Away from the charge neutrality point at $V_G < 0$ side, a constant gap around 30 mV is observed. Near the charge neutrality point, the gap is enhanced to be 73.5 meV, likely due to exchange interaction. **(D)** Left: The tunneling spectra at a low magnetic field B = 5 T. The flat narrow peaks represent LL-like charge excitations with minimum tip gating. The LL filling factor ν and the corresponding orbital numbers are denoted in the top *x*-axis. Right: The dI/dV spectrum at filling factor ν = -1/2 at B = 5 T (linecut in the left panel indicated by the red dashed line) and B = 10 T respectively, with a horizontal offset for clarity. Each peak is labeled by its corresponding orbital number *N*.

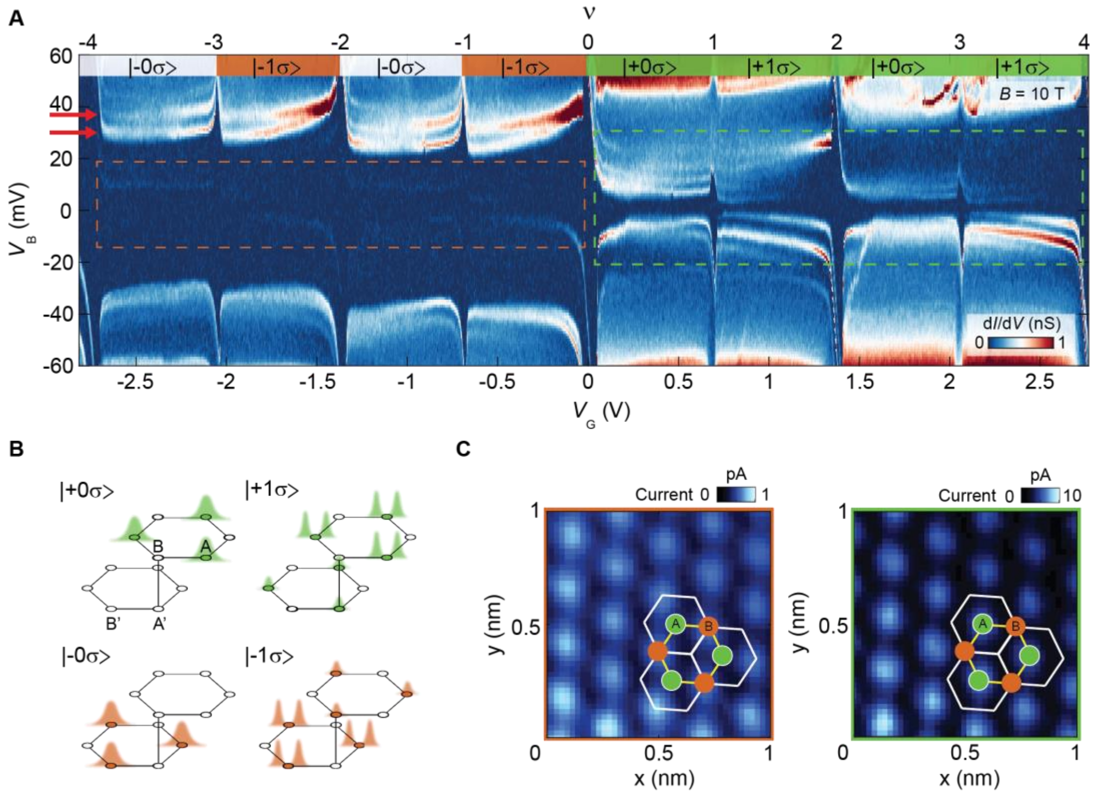

Fig. 2. Atomic wave function imaging of layer polarized N = 0, 1 Landau levels at B = 10 T. **(A)** The tunneling spectra of the lowest Landau levels (LLLs) at magnetic field B = 10 T. The isospin flavors of each LL being filled at the Fermi level are labeled by their corresponding quantum numbers of valley (+, -), orbital number (N = 0, 1), and spin (σ). **(B)** The atomic wave function of the LLLs with different isospin flavors in BLG. The four atomic sites in the unit cell (A, B, A', B') are labeled. **(C)** Atomically-resolved wave function images with sublattice polarization. Left: B sublattice polarized (dimer site on the top layer, in orange) measured at V_B = 96 mV, ν = -4. Right: A sublattice polarized (non-dimer site on the top layer, in green) measured at V_B = 144 mV, ν = -4. Low energy charge excitations in panel **(A)** are grouped by their corresponding sublattice polarization using the same color scheme (green and orange dashed box).

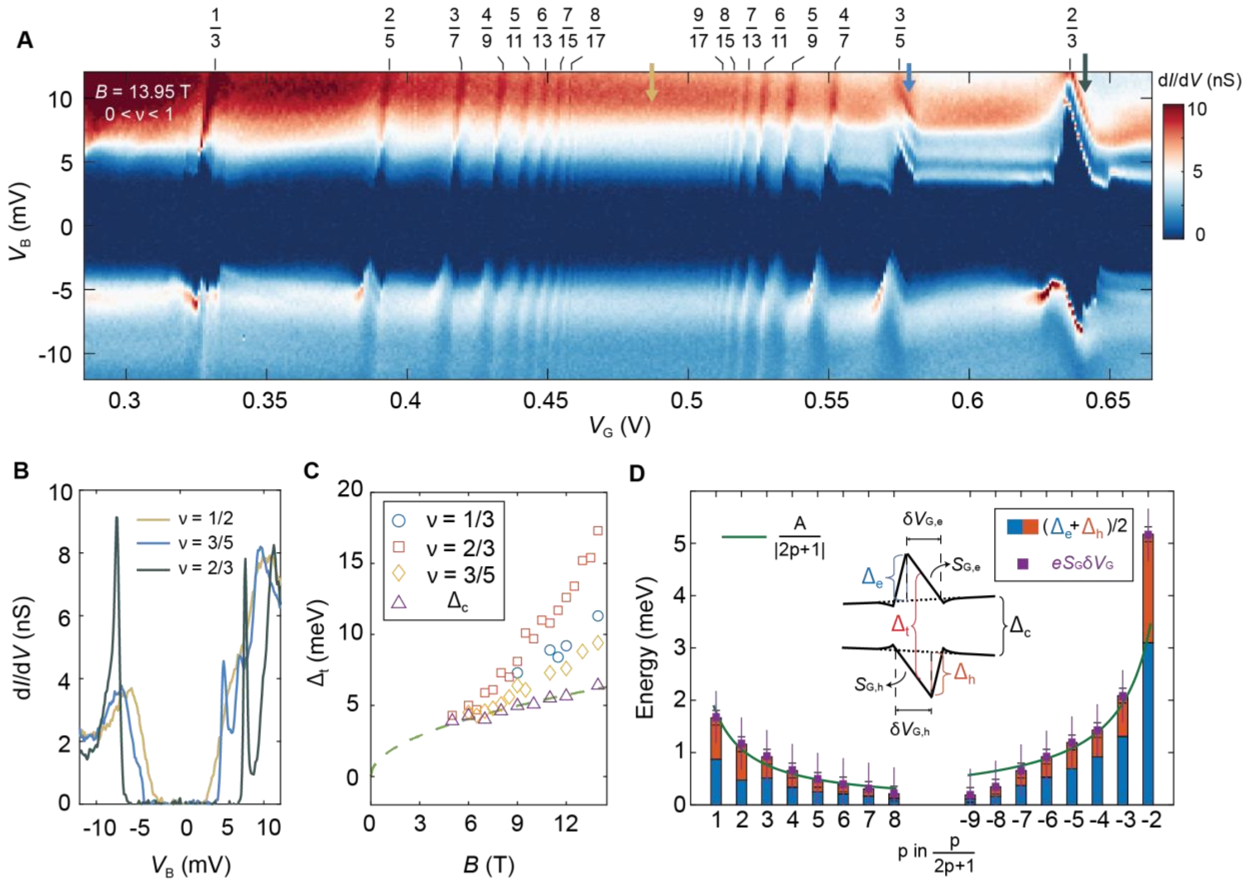

Fig. 3. FQH states within 0 < ν < 1 in the N = 0 LL. (A) The tunneling spectra of the N = 0 LL within $0 < \nu < 1$ at magnetic field B = 13.95 T. FQH states following the Jain sequence up to ν = 8/17 and 9/17 are denoted on the top. **(B)** The tunneling spectra at ν = 1/2, and inside the ν = 3/5 and 2/3 FQH states, indicated by the arrows in panel **(A)**. **(C)** The extracted tunneling gaps Δ_t of FQH states ν = 1/3, 2/3, and 3/5 at different magnetic fields B. The Coulomb gap Δ_C at different magnetic fields is also measured and follows the trend of $\Delta_C \propto \sqrt{B}$ (green dashed line). **(D)** The FQH states local gaps extracted at filling factor $\nu = \frac{p}{2p+1}$ in the N = 0 LL. $(\Delta_e+\Delta_h)/2$ represents the averaged extra excitation energy required to add an electron or a hole to the incompressible FQH states respectively. The blue bars and orange bars represent the portion of the additional energy for an electron and hole respectively. The green solid lines show the fitted $\Delta_e + \Delta_h$ following the trend, $\Delta_e + \Delta_h \propto \frac{1}{|2p+1|}$. We exclude ν = 2/3 in the fitting as it has an abnormally large gap. The averaged gate width $S_G\delta V_G = (S_{G,e}\delta V_{G,e} + S_{G,h}\delta V_{G,h})/2$ (purple squares) of the incompressible FQH states captures the lower bound of the thermodynamic gap $\delta\mu \cong eS_G\delta V_G$. The inset shows the schematic of the local gaps. Error bars are added to represent the measurement's resolution.

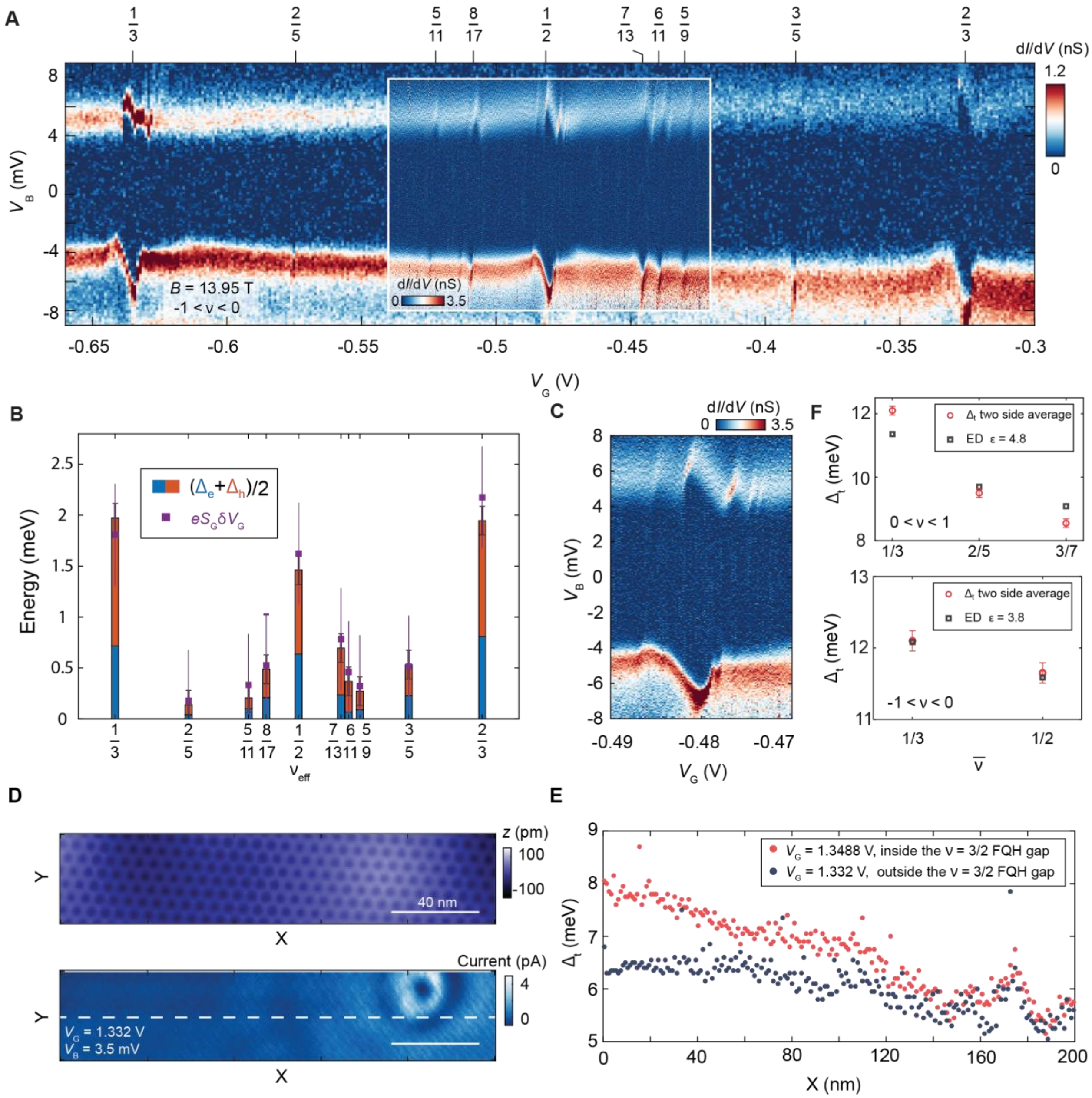

Fig. 4. FQH states in the N = 1 LL. (A) The tunneling spectra of the N = 1 LL within $-1 < \nu < 0$ at magnetic field B = 13.95 T. The corresponding effective fillings factor $\nu_{eff} = \nu - \lfloor \nu \rfloor$ of each FQH state is denoted on the top. Inset is the zoom-in high-resolution spectra near ν_{eff} = 1/2. **(B)** The local gaps $(\Delta_e + \Delta_h)/2$ (blue and orange bars), and the lower bound of the thermodynamic gap $S_G \delta V_G = (S_{G,e}\delta V_{G,e} + S_{G,h}\delta V_{G,h})/2$ (purple squares) of the FQH states observed in panel **(A)**. Here, error bars are added to represent the measurements resolution. **(C)** The zoom-in tunneling spectra near ν_{eff} = 1/2 show the even-denominator FQH state with a large thermodynamic gap $eS_G \delta V_G$~18.9 K. (**D**) Topography image (V_B = 0.4V, I = 3pA) of a 40 nm by 200 nm clean area. The tunneling current map is taken at setpoint V_B = 3.5 mV, I = 1 nA following the trajectory recorded at V_B = 200 mV, I = 1 nA at V_G = 1.332 V in the same location

as shown in the top panel. The current map reveals disorder with ring-like structures around it. **(E)** The spatial variation of the extracted tunneling threshold gap Δ_t across the linecut (white dashed line in panel D), at two specific gate voltage inside/outside (red/blue) the gap feature of ν = 3/2 FQH state in another N = 1 LL. Both D and F are measured at B = 13.2 T. **(F)** Comparison between the measured tunneling gaps Δ_t (red circles) in the middle of the gap feature and the exact diagonalization (ED) calculations (black squares) for FQH states at $0 < \nu < 1$ in the N = 0 LL (top) and $-1 < \nu < 0$ in the N = 1 LL (bottom). The dielectric constants are determined to be ϵ = 4.8 and ϵ = 3.8 respectively (see SI for details). The tunneling gaps Δ_t at ν are averaged result at ν_{eff} and $1 - \nu_{eff}$ (except ν_{eff} = 1/2) to reach a fair comparison with the ED calculations, which assume particle-hole symmetry. Here, error bars are added to represent the measurement's resolution.

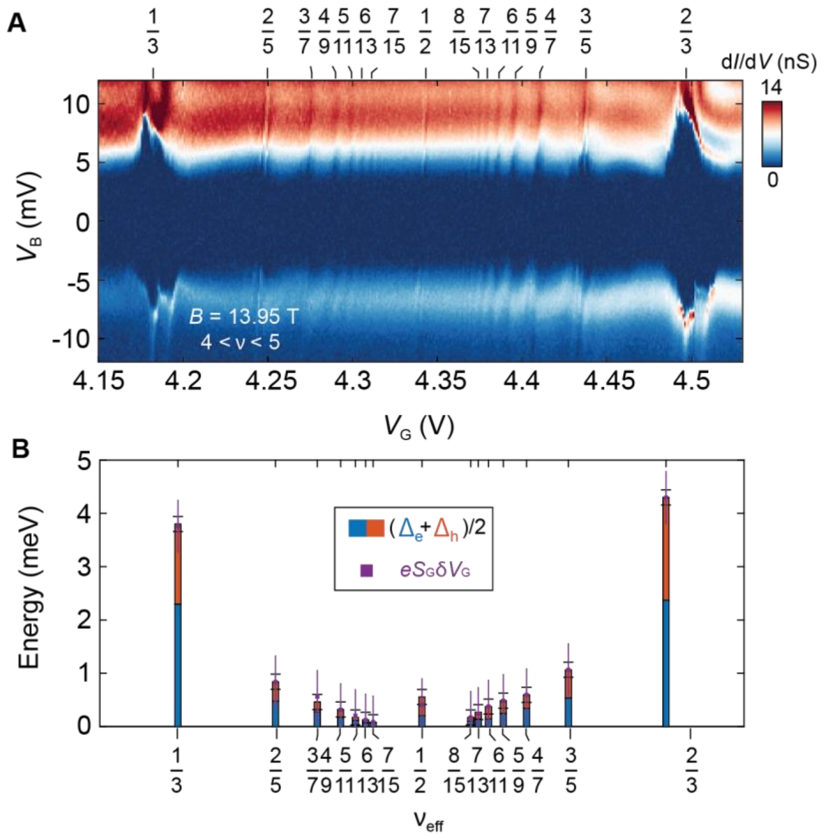

Fig. 5. FQH states within 4 < ν < 5 in the *N* = 2 LL. (A) The tunneling spectra of the *N* = 2 LL within $4 < \nu < 5$. A series of odd-denominator FQH states in the sequence of $\nu_{eff} = \frac{p}{2p+1}$ up to 7/15 and 8/15, and an even-denominator FQH state at ν_{eff} = 1/2 are observed, as denoted on the top. **(B)** The FQH states local gaps extracted in the *N* = 2 LL. $(\Delta_e+\Delta_h)/2$ (blue and orange bars) and the lower bound of the thermodynamic gap $S_G\delta V_G = (S_{G,e}\delta V_{G,e} + S_{G,h}\delta V_{G,h})/2$ (purple squares) are defined following same schematic shown in Figure 3 and Figure 4. Error bars are added to represent the measurement's resolution.